Center-of-Mass and Attitude Control of an Orbital Manipulator: A Novel Control Strategy

Francesco Sena[1], Ria Vijayan[1], Hrishik Mishra[1], and Marco De Stefano[1]

***Abstract*—In this work, we propose a novel control strategy for the displacement of an orbital manipulator equipped with a thruster module at its end-effector. In contrast to the use of base-mounted thrusters, which often leads to allocation problems and fuel inefficiencies, the proposed approach achieves center-of-mass (CoM) maneuvers using only the end-effector thruster. The main challenge is to translate the CoM while maintaining the satellite base attitude fixed and avoiding angular momentum generation.**

The strategy consists of two phases: first, the manipulator orients the thruster while maintaining the base orientation via reaction wheels; second, the thruster generates an external force required to relocate the CoM while conserving attitude. This coordinated use of manipulator motion and end-effector actuation enables effective CoM control under attitude constraints. The proposed controller is validated with multi-body dynamic simulations and an Hardware-in-the-Loop robotic facility.

***Index Terms*—Space Robotics and Automation, Dynamics, Control, Hardware-in-the-Loop, On-Orbit Servicing**

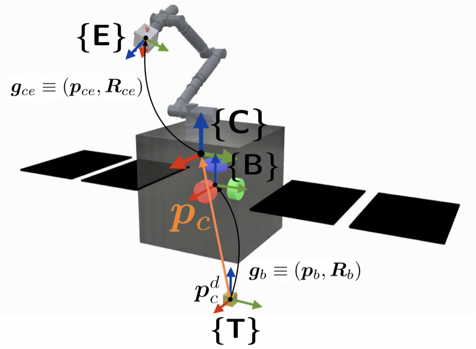

Fig. 1: Relevant frames and kinematic quantities of the orbital manipulator (CAESAR arm [12]) equipped with a thruster module at its end-effector. Color code RGB = XYZ.

I. INTRODUCTION

ROBOTIC on-orbit servicing (OOS) missions [1], [2] are a key asset for the long-term sustainability of space operations [3]. These missions involve a servicing spacecraft, referred to as the *chaser*, equipped with a robotic manipulator (see Fig. 1) that approaches and interacts with a *target* satellite to perform tasks such as inspection, refueling, assembly, or manufacturing [4], [5].

The chaser controls its motion through multiple thrusters [6] and momentum-exchange devices, such as reaction wheels, rigidly mounted on the satellite base [7]. Reaction wheels generate internal torques for attitude control, while thrusters produce external wrenches (forces and torques) acting on the system's center of mass (CoM). Consequently, CoM maneuvers are accomplished by allocating the commanded wrench among the different thrusters, introducing a nonlinear, configuration-dependent allocation problem [8]. Further, since the base orientation is often constrained by communication and payload-pointing requirements [3], [9], the chaser cannot freely reorient, reducing attitude maneuverability and potentially increasing fuel consumption [9].

The control of the CoM dynamics through base actuation is a well-explored research topic [7], [10]. However, CoM control can be also obtained by exploiting the manipulator and thruster actuation together. A standardized thruster-equipped module such as the ORU-AUT [5], [11] can be mounted on the robot end-effector indeed. Several contributions uses this concept: e.g. [13] demonstrates the use of a thruster-powered device at a robot end-effector to regulate whole-body CoM motion, and the Eutelsat 172B design [14] paved the way for in-orbit solutions as [15] that consider end-effector thrusting for navigation and station-keeping.

In particular, the work [16] applies the end-effector thruster concept to achieve CoM relocation: the manipulator reorients its joints to position the thruster module respect to the CoM, while the module translates the entire chaser. By regulating the internal pose to align the thrust direction, the approach reduces, though does not completely eliminate, the angular momentum imparted to the system and achieves CoM translation with no use of the many base thrusters.

While [16] illustrates the advantages of using an end-effector thruster module for CoM control in OOS scenarios, it does not address active regulation of the satellite base.
In this work, we address mission scenarios where there can be stringent requirements on the attitude de-pointing that can be respected despite the dynamic coupling from the motion of the arm displacing the base [7], [12], [17]. In contrast with [16], the work objective is to fill this gap by proposing a control strategy that simultaneously exploits end-effector and manipulator actuation while guaranteeing base-attitude regulation and avoiding angular momentum generation. The contribution is a two-phase control strategy: first, the manipulator aligns the end-effector along a desired direction while the base attitude is actively regulated and reaction-wheel momentum is damped;

Manuscript received: November, 13, 2025; Revised February, 19, 2026; Accepted March, 22, 2026. A video accompanies this manuscript.

This article was recommended for publication by Editor Soon-Jo Chung upon evaluation of the Associate Editor and Reviewers' comments. *(Corresponding author: Francesco Sena)*

[1] Francesco Sena, Ria Vijayan, Hrishik Mishra and Marco De Stefano are with the Institute of Robotics and Mechatronics, German Aerospace Center (DLR), 82234 Wessling, Germany `francesco.sena@dlr.de`

Digital Object Identifier (DOI): see top of this page.

©2026 IEEE. Personal use of this material is permitted. Permission from IEEE must be obtained for all other uses, in any current or future media, including reprinting/republishing this material for advertising or promotional purposes, creating new collective works, for resale or redistribution to servers or lists, or reuse of any copyrighted component of this work in other works. DOI: https://doi.org/10.1109/LRA.2026.3682621

then, the end-effector thruster is used to move the system CoM to the target, with the internal pose maintained (see Fig. 1).

The paper is organized as follows: Sec. II describes the chaser model and its dynamic formulation. Sec. III presents the proposed control strategy and its stability analysis. Sec. IV and Sec. V report the simulation and experimental results, respectively. The attached supplementary video offers a visual demonstration of the experimental results. Finally, Sec. VI concludes the paper.

II. SYSTEM DESCRIPTION AND DYNAMICS

This section defines the notation and frames used throughout the paper and it presents the system dynamics model.

1) Preliminaries: Mathematical functions and notation are hereafter described. The skew-symmetric $so(3)$ algebra is introduced as $S(\bullet) : \mathbb{R}^3 \to so(3)$. The L_2-norm of a vector $\boldsymbol{v} \in \mathbb{R}^n$ is defined $\| \bullet \| : \mathbb{R}^n \to \mathbb{R}$. The symbol $\triangleq$ is used for definition, while $\|$ and $\perp$ are used as subscripts for quantities whose alignment or orthogonality with a certain direction is relevant. The quantity $\boldsymbol{I}_m \in \mathbb{R}^{m\times m}$ denotes an identity matrix of dimension m, while $\boldsymbol{0}_{m,n} \in \mathbb{R}^{m\times n}$ is the zero-element matrix. Indices will be omitted for clarity, when dimensions are evident. The selector matrices are defined as $\boldsymbol{S}_1 \triangleq (\boldsymbol{I}_3,\, \boldsymbol{0}_{3,3})$ and $\boldsymbol{S}_2 \triangleq (\boldsymbol{0}_{3,3},\, \boldsymbol{I}_3)$ and used to extract the linear or the angular parts of a variable.

Relevant notation on the $SE(3)$ group is also recalled for later use in the system motion description. Given a reference frame $\{\mathsf{I}\}$ and a body associated with a frame $\{\mathsf{J}\}$, the body rigid motion can be described as an element of the $SE(3)$ group $\boldsymbol{g}_{ij} \equiv (\boldsymbol{p}_{ij}, \boldsymbol{R}_{ij}) \in SE(3)$, where $\boldsymbol{p}_{ij} \in \mathbb{R}^3$ is the relative position vector and $\boldsymbol{R}_{ij} = [\hat{\boldsymbol{a}}_{ij1}, \hat{\boldsymbol{a}}_{ij2}, \hat{\boldsymbol{a}}_{ij3}] \in SO(3)$ is the relative orientation matrix. Each versor $\hat{\boldsymbol{a}}_{ij\#}$ denotes the $\#$-th coordinate in $\{\mathsf{I}\}$ frame collinear to the $\{\mathsf{J}\}$ axes. The relative body twist is represented as $\boldsymbol{V}_{ij} = (\boldsymbol{v}_{ij}^T,\, \boldsymbol{\omega}_{ij}^T)^T \in \mathbb{R}^6$ where $\boldsymbol{v}_{ij}, \boldsymbol{\omega}_{ij} \in \mathbb{R}^3$ are the linear and angular velocities, respectively. Only one subscript is used when $\{\mathsf{I}\}$ is inertial.

The Adjoint operator $\boldsymbol{Ad}_{ij} : \mathbb{R}^6 \to \mathbb{R}^6$, associated with the relative pose $\boldsymbol{g}_{ij}$, is introduced to map the $\{\mathsf{J}\}$ body coordinates into the $\{\mathsf{I}\}$ frame as follows: $\boldsymbol{Ad}_{ij} = \begin{bmatrix} \boldsymbol{R}_{ij} & \boldsymbol{S}(\boldsymbol{p}_{ij})\boldsymbol{R}_{ij} \\ \boldsymbol{0} & \boldsymbol{R}_{ij} \end{bmatrix}$ [18]. The Adjoint transformation $\boldsymbol{Ad}_{ij}$ maps twists from the $\{\mathsf{J}\}$-frame to $\{\mathsf{I}\}$-frame, and its transpose maps wrenches, which let us compute the relative velocity between two different frames as $\boldsymbol{V}_{ij} = \boldsymbol{V}_j - \boldsymbol{Ad}_{ij}^{-1}\boldsymbol{V}_i$, given their inertial velocities $\boldsymbol{V}_i$ and $\boldsymbol{V}_j$. The $\boldsymbol{Ad}_{ib}$ and $\boldsymbol{Ad}_{eb}$ matrices denote the Adjoint maps from the base to the generic i^{th} body of the chain and to the end-effector, respectively, where the subscripts specify the frames and bodies involved. The i^{th}-body twist $\boldsymbol{V}_i = \boldsymbol{Ad}_{ib}\boldsymbol{V}_b + \boldsymbol{J}_{im}\dot{\boldsymbol{q}}_m$, where the body Jacobian $\boldsymbol{J}_{im} \in \mathbb{R}^{6\times n_m}$ is the standard manipulator Jacobian, while for the end-effector, the well-known form for $\boldsymbol{V}_e = (\boldsymbol{v}_e^T,\, \boldsymbol{\omega}_e^T)^T$ is:

$$\boldsymbol{V}_e = \boldsymbol{Ad}_{eb}\boldsymbol{V}_b + \boldsymbol{J}_{em}\dot{\boldsymbol{q}}_m \tag{1}$$

once the end-effector Jacobian $\boldsymbol{J}_{em}$ is specified.

2) System Modeling and Dynamics: We consider a system comprising of a satellite base equipped with n_r reaction wheels and a robotic manipulator of n_m joints, which has a thrusting module mounted at the manipulator's end-effector.

The system configuration is described as $(\boldsymbol{g}_b,\, \boldsymbol{q}_m,\, \boldsymbol{q}_r) \in SE(3)\times\mathbb{R}^{n_m}\times\mathbb{R}^{n_r}$, where $\boldsymbol{g}_b \in SE(3)$ represents the satellite pose, $\boldsymbol{q}_m \in \mathbb{R}^{n_m}$ denotes the manipulator joints and $\boldsymbol{q}_r \in \mathbb{R}^{n_r}$ corresponds to the reaction wheels' joints.

Fig. 1 illustrates the full system along with the relevant coordinate frames. The orbital frame $\{\mathsf{T}\}$ is assumed to be inertial and located at the origin (e.g. target location $\boldsymbol{p}_c^d$). The frame $\{\mathsf{C}\}$, inertial and aligned with the target frame, marks the center of mass (CoM) of the entire multi-body system (satellite with manipulator), and is located at $\boldsymbol{p}_c$. The body frame $\{\mathsf{B}\}$ is located at the satellite's CoM and aligned with the base's principal axes of inertia. The frame $\{\mathsf{E}\}$ is attached to the manipulator's end-effector, where the thruster is mounted.

The complete system dynamics is expressed in terms of its system velocities $\boldsymbol{V}_S \triangleq (\boldsymbol{V}_b^T,\, \dot{\boldsymbol{q}}_m^T,\, \dot{\boldsymbol{q}}_r^T)^T$, where $\boldsymbol{V}_b = (\boldsymbol{v}_b^T,\, \boldsymbol{\omega}_b^T)^T \in \mathbb{R}^6$ denotes the linear and angular satellite velocities in the $\{\mathsf{T}\}$ frame.

$$\boldsymbol{M}_S\dot{\boldsymbol{V}}_S + \boldsymbol{C}_S(\boldsymbol{V}_S)\boldsymbol{V}_S = \boldsymbol{F}_S \qquad \boldsymbol{F}_S = \begin{bmatrix} \boldsymbol{F}_b + \boldsymbol{Ad}_{eb}^T\boldsymbol{F}_e \\ \boldsymbol{\tau}_m + \boldsymbol{J}_{em}^T\boldsymbol{F}_e \\ \boldsymbol{\tau}_r \end{bmatrix} \tag{2}$$

Here, $\boldsymbol{M}_S \in \mathbb{R}^{(6+n_m+n_r)\times(6+n_m+n_r)}$ denotes the system inertia matrix, while $\boldsymbol{C}_S \in \mathbb{R}^{(6+n_m+n_r)\times(6+n_m+n_r)}$ is the system centrifugal-Coriolis (CC) matrix. The vector $\boldsymbol{F}_S$ represents the system actuation mapped in the $\boldsymbol{V}_S$ dynamics. The terms $\boldsymbol{F}_b \in \mathbb{R}^6$ and $\boldsymbol{F}_e \in \mathbb{R}^6$ denote the external wrenches applied at the frames $\{\mathsf{B}\}$ and $\{\mathsf{E}\}$, respectively. The vectors $\boldsymbol{\tau}_m \in \mathbb{R}^{n_m}$ and $\boldsymbol{\tau}_r \in \mathbb{R}^{n_r}$ correspond to the internal torques of the manipulator and the wheels.

Each wheel is mounted along an axis $\hat{\boldsymbol{a}}_{br,j}$, with $j \in 1,..,n_r$, defined relative to the satellite base's principal axes. Their effect on the system is characterised by their inertia $\boldsymbol{I}_r$ along their spinning axes and by the kinematic projection of these axes into $\{\mathsf{B}\}$, represented by the mapping $\boldsymbol{A} = (\hat{\boldsymbol{a}}_{br,1},\, ...,\, \hat{\boldsymbol{a}}_{br,n_r})$ [17].

This is thoroughly visible in the components of the mass matrix $\boldsymbol{M}_S$, hereafter expanded to introduce quantities we will refer later:

$$\boldsymbol{M}_S = \begin{bmatrix} \boldsymbol{M}_b & \boldsymbol{M}_{bm} & \boldsymbol{M}_{br} \\ \boldsymbol{M}_{bm}^T & \boldsymbol{M}_m & \boldsymbol{0} \\ \boldsymbol{M}_{br}^T & \boldsymbol{0} & \boldsymbol{M}_r \end{bmatrix} \tag{3}$$

The sub-matrices $\boldsymbol{M}_b \in \mathbb{R}^{6\times 6}, \boldsymbol{M}_m \in \mathbb{R}^{n_m\times n_m}, \boldsymbol{M}_r = \boldsymbol{A}^T\boldsymbol{I}_r\boldsymbol{A} \in \mathbb{R}^{n_r\times n_r}$ denote the system locked inertia, the manipulator inertia and the reaction wheels inertia, respectively. The sub-matrices $\boldsymbol{M}_{bm} \in \mathbb{R}^{6\times n_m}$ and $\boldsymbol{M}_{br} = (\boldsymbol{0}^T,\, (\boldsymbol{I}_r\boldsymbol{A})^T)^T \in \mathbb{R}^{6\times n_r}$ define the base-manipulator and base-wheels coupling inertia.

The system linear $\boldsymbol{P}_c \in \mathbb{R}^3$ and angular $\boldsymbol{L}_c \in \mathbb{R}^3$ momentum are also introduced in $\{\mathsf{C}\}$ coordinates:

$$\begin{aligned} \begin{bmatrix} \boldsymbol{P}_c \\ \boldsymbol{L}_c \end{bmatrix} &= \boldsymbol{Ad}_{cb}^{-T}(\boldsymbol{M}_b\boldsymbol{V}_b + \boldsymbol{M}_{bm}\dot{\boldsymbol{q}}_m + \boldsymbol{M}_{br}\dot{\boldsymbol{q}}_r) \\ &= \boldsymbol{Ad}_{cb}^{-T}\boldsymbol{M}_b(\boldsymbol{V}_b + \mathbb{A}_m\dot{\boldsymbol{q}}_m + \mathbb{A}_r\dot{\boldsymbol{q}}_r) \end{aligned} \tag{4}$$

where we define the dynamic-coupling matrices of the satellite-base with the manipulator and the reaction wheels, respectively:

$$\mathbb{A}_m \triangleq \boldsymbol{M}_b^{-1}\boldsymbol{M}_{bm} \qquad \mathbb{A}_r \triangleq \boldsymbol{M}_b^{-1}\boldsymbol{M}_{br} \tag{5}$$

These terms quantify the dynamic reaction of the floating-base in response to the motion of the joints (or the wheels) while the wheels (or the joints) velocities are null and no external wrench is acting on the system. For convenience in subsequent calculations, we define their *angular* components as $\mathbb{A}_{m\omega} \triangleq \boldsymbol{S}_2\mathbb{A}_m$ and $\mathbb{A}_{r\omega} \triangleq \boldsymbol{S}_2\mathbb{A}_r$.

The standard generalized Jacobian [19] of the manipulator $\boldsymbol{J}_{em}^* \in \mathbb{R}^{6\times n_m}$ is also introduced:

$$\boldsymbol{J}_{em}^* \triangleq \boldsymbol{J}_{em} - \boldsymbol{Ad}_{eb}\mathbb{A}_m \qquad \boldsymbol{J}_{er}^* \triangleq -\boldsymbol{Ad}_{eb}\mathbb{A}_r \tag{6}$$

where $\boldsymbol{J}_{er}^* \in \mathbb{R}^{6\times n_r}$ is the correspondent generalized quantity for the wheels. These Jacobians map the joint and wheel velocities into the internal velocity of the end-effector, which is the part of the end-effector velocity that is independent of any external momentum. For clarity in later sections, we express their *linear* parts as $\boldsymbol{J}_{emv}^* \triangleq \boldsymbol{S}_1\boldsymbol{J}_{em}^*$, $\boldsymbol{J}_{erv}^* \triangleq \boldsymbol{S}_1\boldsymbol{J}_{er}^*$.

To proceed with the mathematical formulation, we state the following assumptions:

Assumption 1: The system considered has no external forces and torques actuated by the satellite base, namely $\boldsymbol{F}_b = \boldsymbol{0}$. Initially, the system has null linear $\boldsymbol{P}_c^0 = \boldsymbol{0}$ and angular $\boldsymbol{L}_c^0 = \boldsymbol{0}$ momentum.

Assumption 2: The thruster module at the end-effector provides a continuous bidirectional thrust vector $\boldsymbol{f}_e = [f_{ex},\, f_{ey},\, f_{ez}]^T \in \mathbb{R}^3$ along its own axes applied at $\{\mathsf{E}\}$.

The vector $\boldsymbol{f}_e$ is mapped into the system dynamics as a wrench $\boldsymbol{F}_e = \boldsymbol{S}_1^T\boldsymbol{f}_e \in \mathbb{R}^6$, which consists solely of force components, making the system unable to command an arbitrary external angular motion.

Given the end-effector linear velocity $\boldsymbol{v}_e$ from (1), we rewrite the system dynamics in terms of the actuator velocities $\boldsymbol{V}_A \triangleq (\boldsymbol{v}_e^T,\, \dot{\boldsymbol{q}}_m^T,\, \dot{\boldsymbol{q}}_r^T)^T \in \mathbb{R}^{(3+n_m+n_r)}$ expanded with $\boldsymbol{L}_c$, from (4). Thus, we define $\bar{\boldsymbol{V}}_A \triangleq (\boldsymbol{V}_A^T,\, \boldsymbol{L}_c^T)^T = \boldsymbol{T}_{AS}\boldsymbol{V}_S \in \mathbb{R}^{(6+n_m+n_r)}$. Defining $\boldsymbol{Ad}_\omega \triangleq \boldsymbol{S}_2\boldsymbol{Ad}_{cb}^{-T}$ for readability:

$$\underbrace{\begin{bmatrix} \boldsymbol{v}_e \\ \dot{\boldsymbol{q}}_m \\ \dot{\boldsymbol{q}}_r \\ \boldsymbol{L}_c \end{bmatrix}}_{\bar{\boldsymbol{V}}_A} = \underbrace{\begin{bmatrix} \boldsymbol{S}_1\boldsymbol{Ad}_{eb} & \boldsymbol{S}_1\boldsymbol{J}_{em} & \boldsymbol{0} \\ \boldsymbol{0} & \boldsymbol{I} & \boldsymbol{0} \\ \boldsymbol{0} & \boldsymbol{0} & \boldsymbol{I} \\ \boldsymbol{Ad}_\omega\boldsymbol{M}_b & \boldsymbol{Ad}_\omega\boldsymbol{M}_{bm} & \boldsymbol{Ad}_\omega\boldsymbol{M}_{br} \end{bmatrix}}_{\boldsymbol{T}_{AS}} \underbrace{\begin{bmatrix} \boldsymbol{V}_b \\ \dot{\boldsymbol{q}}_m \\ \dot{\boldsymbol{q}}_r \end{bmatrix}}_{\boldsymbol{V}_S} \tag{7}$$

where $\boldsymbol{T}_{AS} \in \mathbb{R}^{(6+n_m+n_r)\times(6+n_m+n_r)}$ is introduced. The dynamics in (2) can be mapped into the new velocities:

$$\boldsymbol{M}_A\dot{\bar{\boldsymbol{V}}}_A + \boldsymbol{C}_A(\bar{\boldsymbol{V}}_A)\bar{\boldsymbol{V}}_A = \bar{\boldsymbol{F}}_A \tag{8}$$

where $\boldsymbol{M}_A = \boldsymbol{T}_{AS}^{-T}\boldsymbol{M}_S\boldsymbol{T}_{AS}^{-1} \in \mathbb{R}^{(6+n_m+n_r)\times(6+n_m+n_r)}$ and $\boldsymbol{C}_A = \boldsymbol{T}_{AS}^{-T}\boldsymbol{C}_S\boldsymbol{T}_{AS}^{-1} + \boldsymbol{T}_{AS}^{-T}\boldsymbol{M}_S\dot{\boldsymbol{T}}_{AS}^{-1} \in \mathbb{R}^{(6+n_m+n_r)\times(6+n_m+n_r)}$ are the mass and CC matrices [20], and $\bar{\boldsymbol{F}}_A = \boldsymbol{T}_{AS}^{-T}\boldsymbol{F}_S = (\boldsymbol{F}_A^T,\, \boldsymbol{\tau}_c^T)^T$ contains $\boldsymbol{F}_A \triangleq (\boldsymbol{f}_e^T, \boldsymbol{\tau}_m^T, \boldsymbol{\tau}_r^T)^T \in \mathbb{R}^{(3+n_m+n_r)}$ the system actuation vector and $\boldsymbol{\tau}_c = \boldsymbol{S}_2\boldsymbol{Ad}_{ce}^{-T}\boldsymbol{F}_e = S(\boldsymbol{p}_{ce})\boldsymbol{R}_{ce}\boldsymbol{f}_e$ the torque generated by the external force [16].

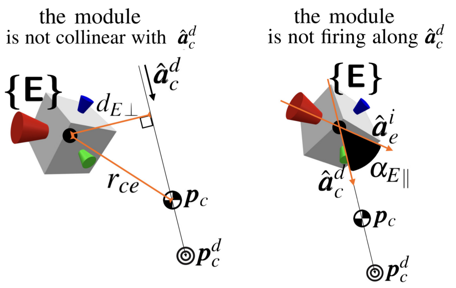

Fig. 2: Alignment parameters r_{ce}, $\alpha_{E\parallel}$, $d_{E\perp}$ representation.

III. PROPOSED CONTROL STRATEGY

In this section, we detail the operational strategy, derive a mapping between task and actuator velocities and design the controller.

1) Operational Strategy: Our task is to coordinate the system actuators to execute a CoM displacement maneuver from $\boldsymbol{p}_c$ to a target location $\boldsymbol{p}_c^d$ (see Fig. 1). In terms of the actuators, we assume:

Assumption 3: Both the manipulator and the reaction wheels are not redundant, namely $n_m = 6$ and $n_r = 3$, and in a singularity-free configuration.

Let $\hat{\boldsymbol{a}}_c^d \triangleq (\boldsymbol{p}_c^d - \boldsymbol{p}_c)/\|\boldsymbol{p}_c^d - \boldsymbol{p}_c\|$ denote the direction from the CoM to the target point. A CoM displacement is achieved by means of the external force $\boldsymbol{f}_e$, which alongside induces an angular momentum change equal to $\dot{\boldsymbol{L}}_c = \boldsymbol{\tau}_c = S(\boldsymbol{p}_{ce})\boldsymbol{R}_{ce}\boldsymbol{f}_e$.

However, the system is under-actuated and not able to generate the external torque to dissipate an arbitrary angular momentum $\boldsymbol{L}_c$, since $\boldsymbol{\tau}_m$ and $\boldsymbol{\tau}_r$ provide internal momentum only. Thus, our strategy aims to conserve $\boldsymbol{L}_c = \mathit{const}$, since $\boldsymbol{L}_c^0 = \boldsymbol{0}$. We generate angular momentum when $S(\boldsymbol{p}_{ce})\boldsymbol{R}_{ce} \neq \boldsymbol{0}$ in two cases: either when the origin of frame $\{\mathsf{E}\}$ is not collinear with the direction vector $\hat{\boldsymbol{a}}_c^d$ (Fig. 2-left) or when the module is not firing along $\hat{\boldsymbol{a}}_c^d$ (Fig. 2-right). Therefore, we divide the maneuver in two sequential steps: first, we align the end-effector's pose around the CoM, $\boldsymbol{g}_{ce}$, along $\hat{\boldsymbol{a}}_c^d$. Once aligned, we move $\boldsymbol{p}_c$.

Alignment Phase. The end-effector is firstly relocated upon $\hat{\boldsymbol{a}}_c^d$, and the firing axis of the thruster module $\hat{\boldsymbol{a}}_e^i$ oriented as $\hat{\boldsymbol{a}}_c^d$, while keeping the satellite attitude $\boldsymbol{R}_b^d \equiv \boldsymbol{R}_b^0$ regulated and the wheels $\boldsymbol{q}_r^d = \mathit{const}$ damped out.

Namely, we impose a constraint on $\{\mathsf{E}\}$ relative position and orientation, $\boldsymbol{g}_{ce}^d = (\boldsymbol{p}_{ce}^d,\, \boldsymbol{R}_{ce}^d)$. This constraint is compliant with three geometrical parameters (see Fig. 2). We introduce:

- the *thruster misalignment* $\alpha_{E\parallel} \triangleq \angle(\hat{\boldsymbol{a}}_e^i, \hat{\boldsymbol{a}}_c^d)$ with respect to the desired direction of CoM motion $\hat{\boldsymbol{a}}_c^d$.
- the *thruster offset* $d_{E\perp} \triangleq ||S(\boldsymbol{p}_{ce})\hat{\boldsymbol{a}}_c^d||$ respect to $\hat{\boldsymbol{a}}_c^d$.
- the *thruster lever arm* $r_{ce} = \|\boldsymbol{p}_{ce}\|$.

The desired lever arm is kept above a minimum safety threshold, namely $r_{ce}^d \geq r_{ce}^{min}$ to avoid firing towards or contacting the satellite base, since the approximation $r_{be}^d \sim r_{ce}^d$ holds due to the high satellite-to-arm mass ratio.

The desired pose $\boldsymbol{g}_{ce}^d \equiv (\boldsymbol{p}_{ce}^d, \boldsymbol{R}_{ce}^d)$ is designed accordingly to the alignment condition $(\alpha_{E\parallel},\, d_{E\perp},\, r_{ce}) \equiv (0, 0, r_{ce}^d)$. The desired relative position is $\boldsymbol{p}_{ce}^d = -r_{ce}^d\hat{\boldsymbol{a}}_c^d$, while the orientation is $\boldsymbol{R}_{ce}^d = [-\hat{\boldsymbol{a}}_c^d,\, \hat{\boldsymbol{a}}_{o3} \wedge (-\hat{\boldsymbol{a}}_c^d),\, (-\hat{\boldsymbol{a}}_c^d) \wedge (\hat{\boldsymbol{a}}_{o3} \wedge (-\hat{\boldsymbol{a}}_c^d))]$

if we assume $\hat{\boldsymbol{a}}_e^i = \hat{\boldsymbol{a}}_e^1$, arbitrarily. Here $\hat{\boldsymbol{a}}_{o3}$ is the unit vector (along z) of the inertial reference frame, i.e. the International Celestial Reference Frame, always defined by having attitude sensor measurements, and it should not parallel to $\hat{\boldsymbol{a}}_c^d$, otherwise one of its two orthogonal axis are used.

Approach Phase. When the alignment is achieved, the approach phase starts. While the force $\boldsymbol{f}_e$ displaces the CoM to $\boldsymbol{p}_c^d$, the torques $\boldsymbol{\tau}_r$ and $\boldsymbol{\tau}_m$ regulate the base orientation and damp out the reaction wheels and joints motion.

2) Dynamic Mapping in Task Velocities: In this subsection, we relate the task velocities, to $\bar{\boldsymbol{V}}_A$, in order to rewrite (8) in the task dynamics.

According to the operational strategy, we target to control the CoM velocity $\boldsymbol{v}_c$, the relative velocity $\boldsymbol{V}_{ce}$, the base angular velocity $\boldsymbol{\omega}_b$ and the wheels velocity $\dot{\boldsymbol{q}}_r$ through $\boldsymbol{F}_A$.

Given (4), the CoM velocity $\boldsymbol{v}_c$, which represents the system's translational motion, is obtained by projecting $\boldsymbol{M}_b$ into the $\{\mathsf{C}\}$ frame and isolating the translational term:

$$\boldsymbol{v}_c = \boldsymbol{S}_1 \boldsymbol{M}_c^{-1} \begin{bmatrix} \boldsymbol{P}_c \\ \boldsymbol{L}_c \end{bmatrix} = \boldsymbol{m}^{-1}\boldsymbol{P}_c \tag{9}$$

where $\boldsymbol{M}_c = \boldsymbol{Ad}_{cb}^{-T}\boldsymbol{M}_b\boldsymbol{Ad}_{cb}^{-1} = \mathit{blkdiag}(\boldsymbol{m}, \boldsymbol{I}_c)$ is employed. Here, $\boldsymbol{m} = m\boldsymbol{I}_3$ represents the system mass and $\boldsymbol{I}_c$ is the inertia matrix expressed in $\{\mathsf{C}\}$ coordinates.

The relative velocity $\boldsymbol{V}_{ce}$ expresses the motion of the end-effector, and of the thruster module, around the system CoM. It can be straightforwardly derived through (1) and (4):

$$\boldsymbol{V}_{ce} = \boldsymbol{V}_e - \boldsymbol{Ad}_{ec} \begin{bmatrix} \boldsymbol{v}_c \\ \boldsymbol{I}_c^{-1}\boldsymbol{L}_c \end{bmatrix} = \boldsymbol{J}_{em}^*\dot{\boldsymbol{q}}_m + \boldsymbol{J}_{er}^*\dot{\boldsymbol{q}}_r \tag{10}$$

where the generalized Jacobians defined in (6) and the expression of $\boldsymbol{M}_c^{-1}(\boldsymbol{P}_c^T, \boldsymbol{L}_c^T)^T$ in terms of $\boldsymbol{v}_c$ and $\boldsymbol{L}_c$ are used.

By extracting the linear equation of (10), we express the CoM velocity $\boldsymbol{v}_c$ in terms of the $\bar{\boldsymbol{V}}_A$ components, as:

$$\boldsymbol{v}_c = \boldsymbol{R}_{ce}\boldsymbol{v}_e - \boldsymbol{R}_{ce}\boldsymbol{J}_{emv}^*\dot{\boldsymbol{q}}_m - \boldsymbol{R}_{ce}\boldsymbol{J}_{erv}^*\dot{\boldsymbol{q}}_r + \underbrace{S(\boldsymbol{p}_{ce})\boldsymbol{I}_c^{-1}}_{\boldsymbol{T}_{vL}}\boldsymbol{L}_c \tag{11}$$

where $\boldsymbol{p}_{ce}$ and $\boldsymbol{R}_{ce}$ represents the $\{\mathsf{E}\}$ position and orientation with respect to $\{\mathsf{C}\}$ and $\boldsymbol{T}_{vL} = S(\boldsymbol{p}_{ce})\boldsymbol{I}_c^{-1}$. From (10), we further derive $\dot{\boldsymbol{q}}_m$ in task velocities:

$$\dot{\boldsymbol{q}}_m = \boldsymbol{J}_{em}^{*-1}\boldsymbol{V}_{ce} - \boldsymbol{J}_{em}^{*-1}\boldsymbol{J}_{er}^*\dot{\boldsymbol{q}}_r \tag{12}$$

The base attitude can be expressed as a combination of $\boldsymbol{V}_{ce}$, $\dot{\boldsymbol{q}}_r$ and $\boldsymbol{L}_c$. Indeed, from (4) and (12), it holds:

$$\begin{aligned}\boldsymbol{\omega}_b = &- \mathbb{A}_{m\omega}\boldsymbol{J}_{em}^{*-1}\boldsymbol{V}_{ce} - (\mathbb{A}_{r\omega} - \mathbb{A}_{m\omega}\boldsymbol{J}_{em}^{*-1}\boldsymbol{J}_{er}^*)\dot{\boldsymbol{q}}_r \\ &+ \boldsymbol{R}_{cb}^{-1}\boldsymbol{I}_c^{-1}\boldsymbol{L}_c\end{aligned} \tag{13}$$

Thus, we define as $\boldsymbol{V}_C \triangleq (\boldsymbol{v}_c^T, \boldsymbol{V}_{ce}^T, \dot{\boldsymbol{q}}_r^T)^T \in \mathbb{R}^{9+n_r}$ the task velocity vector. Before writing the system dynamics in this new velocities, as done previously, we augment $\boldsymbol{V}_C$ with $\boldsymbol{L}_c$ to include the uncontrolled dynamics, such as $\bar{\boldsymbol{V}}_C = (\boldsymbol{V}_C^T, \boldsymbol{L}_c^T)^T \in \mathbb{R}^{12+n_r}$. Recalling (10) and (11), the transformation $\boldsymbol{T}_{CA}$ maps the augmented actuator velocities $\bar{\boldsymbol{V}}_A$ into the augmented task velocities $\bar{\boldsymbol{V}}_C = \boldsymbol{T}_{CA}\bar{\boldsymbol{V}}_A$ as:

$$\underbrace{\begin{bmatrix} \boldsymbol{v}_c \\ \boldsymbol{V}_{ce} \\ \dot{\boldsymbol{q}}_r \\ \boldsymbol{L}_c \end{bmatrix}}_{\bar{\boldsymbol{V}}_C} = \underbrace{\begin{bmatrix} \boldsymbol{R}_{ce} & -\boldsymbol{R}_{ce}\boldsymbol{J}_{emv}^* & -\boldsymbol{R}_{ce}\boldsymbol{J}_{erv}^* & \boldsymbol{T}_{vL} \\ \boldsymbol{0} & \boldsymbol{J}_{em}^* & \boldsymbol{J}_{er}^* & \boldsymbol{0} \\ \boldsymbol{0} & \boldsymbol{0} & \boldsymbol{I} & \boldsymbol{0} \\ \boldsymbol{0} & \boldsymbol{0} & \boldsymbol{0} & \boldsymbol{I} \end{bmatrix}}_{\boldsymbol{T}_{CA}} \underbrace{\begin{bmatrix} \boldsymbol{v}_e \\ \dot{\boldsymbol{q}}_m \\ \dot{\boldsymbol{q}}_r \\ \boldsymbol{L}_c \end{bmatrix}}_{\bar{\boldsymbol{V}}_A} \tag{14}$$

3) Proposed Controller: The system dynamics is now projected through Eq. (14) in terms of the augmented task velocities. We partition the vector $\bar{\boldsymbol{V}}_C = (\boldsymbol{v}_c^T, \boldsymbol{\xi}^T, \boldsymbol{L}_c^T)^T \in \mathbb{R}^{15}$ since the alignment task focuses on $\boldsymbol{\xi} \triangleq (\boldsymbol{V}_{ce}^T, \dot{\boldsymbol{q}}_r^T)^T \in \mathbb{R}^9$ control (and $\boldsymbol{\omega}_b$ via (13)). This partition reflects a decomposition of the system motion: $\boldsymbol{v}_c$ and $\boldsymbol{L}_c$ are associated with the external motion generated by external forces and torques, respectively, whereas $\boldsymbol{\xi}$ represents internal motion induced solely by the internal actuators:

$$\boldsymbol{M}_C \begin{bmatrix} \dot{\boldsymbol{v}}_c \\ \dot{\boldsymbol{\xi}} \\ \dot{\boldsymbol{L}}_c \end{bmatrix} + \boldsymbol{C}_C \underbrace{\begin{bmatrix} \boldsymbol{v}_c \\ \boldsymbol{\xi} \\ \boldsymbol{L}_c \end{bmatrix}}_{\bar{\boldsymbol{V}}_C} = \underbrace{\begin{bmatrix} \boldsymbol{f}_c \\ \boldsymbol{F}_\xi \\ \boldsymbol{\tau}_c \end{bmatrix}}_{\bar{\boldsymbol{F}}_C} \qquad \boldsymbol{F}_\xi \triangleq \begin{bmatrix} \boldsymbol{F}_{ce} \\ \boldsymbol{\tau}_r \end{bmatrix} \tag{15}$$

$$\boldsymbol{M}_C = \text{blkdiag}(\begin{bmatrix} \boldsymbol{m} & \boldsymbol{M}_\xi & \boldsymbol{I} \end{bmatrix})$$

$$\boldsymbol{C}_C = \begin{bmatrix} \boldsymbol{0}_{3,3} & \boldsymbol{C}_{v_c,\xi} & \boldsymbol{C}_{v_c,L_c} \\ -\boldsymbol{C}_{v_c,\xi}^T & \boldsymbol{C}_\xi & \boldsymbol{C}_{\xi,L_c} \\ -\boldsymbol{C}_{v_c,L_c}^T & -\boldsymbol{C}_{\xi,L_c}^T & \boldsymbol{C}_{L_c} \end{bmatrix}$$

deriving the mass $\boldsymbol{M}_C = \boldsymbol{T}_{CA}^{-T}\boldsymbol{M}_A\boldsymbol{T}_{CA}^{-1} \in \mathbb{R}^{15\times 15}$, the CC matrix $\boldsymbol{C}_C = \boldsymbol{T}_{CA}^{-T}\boldsymbol{C}_A\boldsymbol{T}_{CA}^{-1} + \boldsymbol{T}_{CA}^{-T}\boldsymbol{M}_A\dot{\boldsymbol{T}}_{CA}^{-1} \in \mathbb{R}^{15\times 15}$ and the vector $\bar{\boldsymbol{F}}_C = (\boldsymbol{F}_C^T, \boldsymbol{\tau}_c^T)^T = \boldsymbol{T}_{CA}^{-T}\boldsymbol{F}_A$ where $\boldsymbol{F}_C \triangleq (\boldsymbol{f}_c^T, \boldsymbol{F}_\xi^T)^T \in \mathbb{R}^{12}$ is the task control vector. Also, in (15), the passivity property $\bar{\boldsymbol{V}}_C^T(\dot{\boldsymbol{M}}_C - 2\boldsymbol{C}_C)\,\bar{\boldsymbol{V}}_C = 0$ holds [21].

The terms $\boldsymbol{M}_\xi \in \mathbb{R}^{9\times 9}$, $\boldsymbol{C}_\xi \in \mathbb{R}^{9\times 9}$ and $\boldsymbol{F}_\xi \in \mathbb{R}^9$ represent the mass, Coriolis and generalized forces associated to $\boldsymbol{\xi}$. From Netwon's law, $\boldsymbol{m}\dot{\boldsymbol{v}}_c = \boldsymbol{f}_c$. Thus, $\boldsymbol{C}_{v_c,\xi}\boldsymbol{\xi} + \boldsymbol{C}_{v_c,L_c}\boldsymbol{L}_c = \boldsymbol{0}$.

We now define the task errors to design the virtual controllers. The CoM error is $\Delta\boldsymbol{p}_c = \boldsymbol{p}_c - \boldsymbol{p}_c^d$, while we want to damp out the wheels, $\dot{\boldsymbol{q}}_r^d = 0$, namely $\Delta\boldsymbol{q}_r = \boldsymbol{q}_r - \boldsymbol{q}_r^d = \mathit{const}$.

The current $\boldsymbol{g}_{ce}$ and desired $\boldsymbol{g}_{ce}^d$ end-effector poses are expressed using position-quaternion coordinates as $\boldsymbol{X}_{ce} = (\boldsymbol{p}_{ce}^T, 2\boldsymbol{\epsilon}_{ce}^T)^T$, where $\boldsymbol{\epsilon}_{ce}$ and $\boldsymbol{\eta}_{ce}$ are the vector and scalar components of the quaternion associated with $\boldsymbol{R}_{ce}$. The relative pose error is given by $\Delta\boldsymbol{X}_{ce} = (\Delta\boldsymbol{p}_{ce}^T, 2\Delta\boldsymbol{\epsilon}_{ce}^T)^T$, and the mapping matrix $\boldsymbol{E}_{\boldsymbol{X}_{ce}} = \Delta\boldsymbol{\eta}_{ce}\boldsymbol{I}_3 + S(\Delta\boldsymbol{\epsilon}_{ce})$ is introduced [22]. This yields the Jacobian $\boldsymbol{J}_{\boldsymbol{X}_{ce}} = \text{blkdiag}(\boldsymbol{I}_3, \boldsymbol{E}_{\boldsymbol{X}_{ce}}) \in \mathbb{R}^{6\times 6}$, relating pose derivative and velocity via $\dot{\boldsymbol{X}}_{ce} = \boldsymbol{J}_{\boldsymbol{X}_{ce}}\boldsymbol{V}_{ce}$.

Analogously, the attitude error is defined from the current $\boldsymbol{R}_b$ and desired $\boldsymbol{R}_b^d$ rotations, using the error quaternion $(\Delta\boldsymbol{\eta}_b, \Delta\boldsymbol{\epsilon}_b)$, where the matrix $\boldsymbol{E}_{\boldsymbol{X}_b} = \Delta\boldsymbol{\eta}_b\boldsymbol{I}_3 + S(\Delta\boldsymbol{\epsilon}_b)$ maps angular velocity to quaternion rate as $\dot{\boldsymbol{\epsilon}}_b = \boldsymbol{E}_{\boldsymbol{X}_b}\boldsymbol{\omega}_b$.

By recalling Eq. (13) for the base-attitude task, we propose the following task virtual controller:

$$\begin{bmatrix} \boldsymbol{f}_c \\ \boldsymbol{F}_{ce} \\ \boldsymbol{\tau}_r \end{bmatrix}_{task} = \begin{bmatrix} \boldsymbol{f}_{c,PD} \\ \boldsymbol{F}_{ce,PD} - (\mathbb{A}_{m\omega}\boldsymbol{J}_{em}^{*-1})^T\boldsymbol{\tau}_{b,P} \\ \boldsymbol{\tau}_{r,D} - (\mathbb{A}_{r\omega} - \mathbb{A}_{m\omega}\boldsymbol{J}_{em}^{*-1}\boldsymbol{J}_{er}^*)^T\boldsymbol{\tau}_{b,P} \end{bmatrix} \tag{16}$$

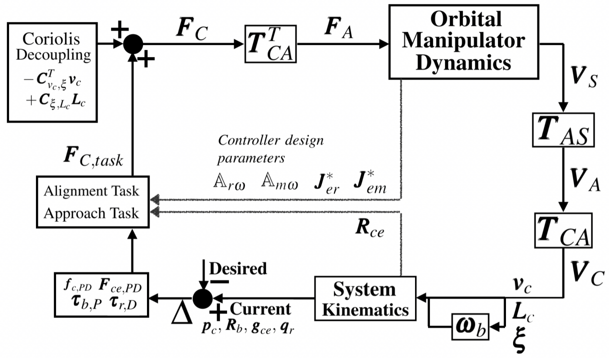

Fig. 3: Block diagram of the proposed controller.

The PD control force acting on the system CoM is defined as $\boldsymbol{f}_{c,\mathrm{PD}} = -\boldsymbol{K}_c\Delta\boldsymbol{p}_c - \boldsymbol{D}_c\boldsymbol{v}_c$, where $\boldsymbol{K}_c \in \mathbb{R}^{3\times3} \succ 0$ and $\boldsymbol{D}_c \in \mathbb{R}^{3\times3} \succ 0$ are the associated stiffness and damping matrices. The PD virtual wrench on the relative end-effector pose is $\boldsymbol{F}_{ce,\mathrm{PD}} = \boldsymbol{F}_{ce,\mathrm{P}} + \boldsymbol{F}_{ce,\mathrm{D}} = -\boldsymbol{J}^T_{X_{ce}}\boldsymbol{K}_{ce}\Delta\boldsymbol{X}_{ce} - \boldsymbol{D}_{ce}\boldsymbol{V}_{ce}$, where $\boldsymbol{K}_{ce} \in \mathbb{R}^{6\times6} \succ 0$ and $\boldsymbol{D}_{ce} \in \mathbb{R}^{6\times6} \succ 0$ are the corresponding gain matrices. The reaction wheels are subject to a damping control law of the form $\boldsymbol{\tau}_{r,\mathrm{D}} = -\boldsymbol{D}_r\dot{\boldsymbol{q}}_r$, with $\boldsymbol{D}_r \in \mathbb{R}^{3\times3} \succ 0$. Finally, the base attitude is regulated via a proportional action on the vector part of the attitude error quaternion $\boldsymbol{\tau}_{b,\mathrm{P}} = -2\boldsymbol{E}^T_{X_b}\boldsymbol{K}_b\Delta\boldsymbol{\epsilon}_b$, where $\boldsymbol{K}_b \in \mathbb{R}^{3\times3} \succ 0$ [22].

The CoM motion is decoupled from the rest of the task coordinates dynamics, therefore $\boldsymbol{f}_c \equiv \boldsymbol{f}_{c,task}$. The dynamic coupling between $\boldsymbol{\xi}$ and $\boldsymbol{v}_c$ and $\boldsymbol{L}_c$ is instead removed from $\boldsymbol{\xi}$ dynamics by adding up to the task controllers defined in Eq. (16), the Coriolis term related to the other components:

$$\boldsymbol{F}_\xi = \begin{bmatrix} \boldsymbol{F}_{ce} \\ \boldsymbol{\tau}_r \end{bmatrix} = \begin{bmatrix} \boldsymbol{F}_{ce} \\ \boldsymbol{\tau}_r \end{bmatrix}_{task} - \boldsymbol{C}^T_{v_c,\xi}\boldsymbol{v}_c + \boldsymbol{C}_{\xi,L_c}\boldsymbol{L}_c \quad (17)$$

Finally, the terms can be projected in the actuation vector $\boldsymbol{F}_A$ through the $\boldsymbol{T}^T_{CA}$ matrix transpose, defined in Eq. (14):

$$\underbrace{\begin{bmatrix} \boldsymbol{f}_e \\ \boldsymbol{\tau}_m \\ \boldsymbol{\tau}_r \end{bmatrix}}_{\boldsymbol{F}_A} = \underbrace{\begin{bmatrix} \mathbf{0} \\ \boldsymbol{J}^{*T}_{em}\boldsymbol{F}_{ce,PD} - \mathbb{A}^T_{m\omega}\boldsymbol{\tau}_{b,P} \\ \boldsymbol{J}^{*T}_{er}\boldsymbol{F}_{ce,PD} + \boldsymbol{\tau}_{r,D} - \mathbb{A}^T_{r\omega}\boldsymbol{\tau}_{b,P} \end{bmatrix}}_{\text{Alignment Task}}$$
$$+ \underbrace{\begin{bmatrix} \boldsymbol{R}^T_{ce}\boldsymbol{f}_{c,PD} \\ (-\boldsymbol{R}_{ce}\boldsymbol{J}^*_{emv})^T\boldsymbol{f}_{c,PD} \\ (-\boldsymbol{R}_{ce}\boldsymbol{J}^*_{erv})^T\boldsymbol{f}_{c,PD} \end{bmatrix}}_{\text{Approach Task}} + \underbrace{\begin{bmatrix} \mathbf{0} \\ \boldsymbol{J}^{*T}_{em}\boldsymbol{c}_{ce} \\ \boldsymbol{J}^{*T}_{er}\boldsymbol{c}_{ce} + \boldsymbol{c}_r \end{bmatrix}}_{\text{Coriolis decoupling}} \quad (18)$$

where $\boldsymbol{c}_{ce} \triangleq -\boldsymbol{C}^T_{v_c,V_{ce}}\boldsymbol{v}_c + \boldsymbol{C}_{V_{ce},L_c}\boldsymbol{L}_c$ and $\boldsymbol{c}_r \triangleq -\boldsymbol{C}^T_{v_c,\dot{q}_r}\boldsymbol{v}_c + \boldsymbol{C}_{\dot{q}_r,L_c}\boldsymbol{L}_c$ are introduced for better readability.

As visible in Eq. (18), the end-effector force $\boldsymbol{f}_e$ controls the CoM independently, while the internal torques $\boldsymbol{\tau}_m$ and $\boldsymbol{\tau}_r$ not only commands the alignment tasks but also compensate for the CoM motion and for the Coriolis decoupling.

Fig. 3 shows a block diagram of the proposed controller where the different relations derived in the paper are linked to each other.

4) Stability Proof: First, we insert the controllers defined in (16) and (17) into (15) to obtain the control loop dynamics. Then, given the kinematic relationships $\Delta\dot{\boldsymbol{p}}_c = \boldsymbol{v}_c$ and $\Delta\dot{\boldsymbol{X}}_{ce} = \boldsymbol{J}_{\boldsymbol{X}_{ce}}\boldsymbol{V}_{ce}$, a first order system in the state-space form $\dot{\bar{\boldsymbol{z}}} = \boldsymbol{f}(\bar{\boldsymbol{z}})$ is derived, where state-space vector $\bar{\boldsymbol{z}} = (\boldsymbol{z}^T, \boldsymbol{L}_c^T)^T \in \bar{\boldsymbol{X}}$ with $\boldsymbol{z} = (\Delta\boldsymbol{p}_c^T, \boldsymbol{v}_c^T, \Delta\boldsymbol{X}_{ce}^T, \boldsymbol{V}_{ce}^T, \Delta\boldsymbol{q}_r^T, \dot{\boldsymbol{q}}_r^T)^T \in \boldsymbol{X}$ is here defined.

Given Assumption 1, $\boldsymbol{L}_c$ remains null during the maneuver. Thus, we proof stability for the control velocities $\boldsymbol{V}_C$ in the system subset $\boldsymbol{z}$ holding this condition.

Let us partition $\boldsymbol{z} = [\boldsymbol{z}_c, \boldsymbol{z}_\xi]$ where $\boldsymbol{z}_c = [\Delta\boldsymbol{p}_c, \boldsymbol{v}_c]$ and $\boldsymbol{z}_\xi = [\Delta\boldsymbol{X}_{ce}, \boldsymbol{V}_{ce}, \Delta\boldsymbol{q}_r, \dot{\boldsymbol{q}}_r]$. The triangular relations $\dot{\boldsymbol{z}}_c = \boldsymbol{f}_1(\boldsymbol{z}_c)$, $\dot{\boldsymbol{z}}_\xi = \boldsymbol{f}_2(\boldsymbol{z}_c, \boldsymbol{z}_\xi)$ can be derived. We can prove the stability considering the two sequential phases of our operational strategy.

Approach Phase. During the approach maneuver, $\dot{\boldsymbol{z}}_c = \boldsymbol{f}(\boldsymbol{z}_c)$ determines CoM motion and it is independent from $\boldsymbol{z}_\xi$. Thus, the control stability can be demonstrated in a cascade fashion through successive convergence to nested subsets similar to [23]: first, we converge to $\boldsymbol{z}_c = \mathbf{0}$ and then we prove stability for $\boldsymbol{z}_\xi$. Considering the following Lyapunov function:

$$T_1 = \frac{1}{2}\boldsymbol{v}_c^T\boldsymbol{m}\boldsymbol{v}_c + \frac{1}{2}\Delta\boldsymbol{p}_c^T\boldsymbol{K}_c\Delta\boldsymbol{p}_c \quad (19)$$

By derivation and using (15) and (16), we obtain:

$$\dot{T}_1 = \frac{1}{2}\boldsymbol{v}_c^T\dot{\boldsymbol{m}}\boldsymbol{v}_c + \boldsymbol{v}_c^T\boldsymbol{m}\dot{\boldsymbol{v}}_c + \boldsymbol{v}_c^T\boldsymbol{K}_c\Delta\boldsymbol{p}_c = -\boldsymbol{v}_c^T\boldsymbol{D}_c\boldsymbol{v}_c \leq 0 \quad (20)$$

Then, applying LaSalle invariance principle, asymptotical stability is proved for $\boldsymbol{z}_c$ with $\boldsymbol{D}_c \succ 0$.

Alignment Phase. The stability of $\dot{\boldsymbol{z}}_\xi = \boldsymbol{f}_2(\mathbf{0}, \boldsymbol{z}_\xi)$ is here demonstrated. Let us introduce $\boldsymbol{X}_\xi$ as the subset of $\boldsymbol{X}$ such that: $\boldsymbol{X}_\xi = \{\boldsymbol{z} | \boldsymbol{z} \in \boldsymbol{X} \land \boldsymbol{z}_c = \mathbf{0}\}$. We choose the subsequent Lyapunov function candidate:

$$T_2 = \frac{1}{2}\boldsymbol{\xi}^T\boldsymbol{M}_\xi\boldsymbol{\xi} + \frac{1}{2}\Delta\boldsymbol{X}_{ce}^T\boldsymbol{K}_{ce}\Delta\boldsymbol{X}_{ce} + \frac{1}{2}(2\Delta\boldsymbol{\epsilon}_b)^T\boldsymbol{K}_b(2\Delta\boldsymbol{\epsilon}_b) \quad (21)$$

By derivation, we obtain an expression for $\dot{T}_2$:

$$\begin{aligned} \dot{T}_2 &= \frac{1}{2}\boldsymbol{\xi}^T\dot{\boldsymbol{M}}_\xi\boldsymbol{\xi} + \boldsymbol{\xi}^T\boldsymbol{M}_\xi\dot{\boldsymbol{\xi}} + \dot{\boldsymbol{X}}_{ce}^T\boldsymbol{K}_{ce}\Delta\boldsymbol{X}_{ce} + \dot{\boldsymbol{\epsilon}}_b^T\boldsymbol{K}_b\Delta\boldsymbol{\epsilon}_b \\ &= \boldsymbol{\xi}^T(\boldsymbol{F}_\xi + \boldsymbol{C}^T_{v_c,\xi}\boldsymbol{v}_c) + \boldsymbol{V}_{ce}^T\boldsymbol{J}^T_{X_{ce}}\boldsymbol{K}_{ce}\Delta\boldsymbol{X}_{ce} \\ &\quad + \boldsymbol{\omega}_b^T 2\boldsymbol{E}^T_{X_b}\boldsymbol{K}_b\Delta\boldsymbol{\epsilon}_b \end{aligned} \quad (22)$$

where we substitute $\boldsymbol{M}_\xi\dot{\boldsymbol{\xi}} = \boldsymbol{F}_\xi - \boldsymbol{C}_\xi\boldsymbol{\xi} + \boldsymbol{C}^T_{v_c,\xi}\boldsymbol{v}_c$ ($\boldsymbol{L}_c = \mathbf{0}$) from Eqs. (15) and (17) and apply the passivity property of the Euler Lagrange systems $\boldsymbol{\xi}^T(\frac{1}{2}\dot{\boldsymbol{M}}_\xi - \boldsymbol{C}_\xi)\boldsymbol{\xi} = 0$ [21].

Using Eq. (13) to express $\boldsymbol{\omega}_b$ in task coordinates and Eq. (17) to explicit our controller, we obtain:

$$\begin{aligned} \dot{T}_2 &= \boldsymbol{\xi}^T\boldsymbol{F}_{\xi,task} + \dot{\boldsymbol{q}}_r^T(\mathbb{A}_{r\omega} - \mathbb{A}_{m\omega}\boldsymbol{J}^{*-1}_{em}\boldsymbol{J}^*_{er})^T\boldsymbol{\tau}_{P,b} \\ &\quad + \boldsymbol{V}_{ce}^T\boldsymbol{F}_{ce,P} + \boldsymbol{V}_{ce}^T(\mathbb{A}_{m\omega}\boldsymbol{J}^{*-1}_{em})^T\boldsymbol{\tau}_{P,b} \\ &= -\boldsymbol{V}_{ce}^T\boldsymbol{D}_{ce}\boldsymbol{V}_{ce} - \dot{\boldsymbol{q}}_r^T\boldsymbol{D}_r\dot{\boldsymbol{q}}_r \leq 0 \end{aligned} \quad (23)$$

leading to cascade stability [23] once the task convergence is met. Thus, by applying standard LaSalle arguments, asymptotical stability also follows.

IV. NUMERICAL EXPERIMENTS

This section details the simulation tests done to validate the proposed control strategy, performed in a MATLAB-Simulink environment. A 6 Degree-of-Freedom (DoF) manipulator is mounted on the base. The thruster module provides continuous thrust along three orthogonal directions, with $\hat{\boldsymbol{a}}^1_{ce}$ as the main thrusting direction. All linear and angular velocities are initialized to zero, and the system is assumed to start with zero total momentum. The relevant reference frames are illustrated in Fig. 1 and the simulation parameters specified in Table I.

Throughout the simulation, the orientation is represented using Euler angles $\boldsymbol{\phi} = (\alpha, \beta, \gamma)$ (XYZ convention) and each pose error denoted as $(\Delta\boldsymbol{p}, \Delta\boldsymbol{\phi})$ at convenience.

To validate the controller performance across the two operational phases, the results are generated from a sequentially executed trajectory. However, each phase is discussed independently to highlight the effectiveness of the control actions specific to each task.

TABLE I: Dynamic and control parameters used for the validation.

Parameter	**Numerical**	**Experiment**
m $[kg]$	2000	400
$\boldsymbol{I}_b$ $[kgm^2]$	diag([508, 508, 508])	diag([360, 363, 265])
$\boldsymbol{I}_r$ $[kgm^2]$	diag([0.04,0.04,0.04])	diag([0.04,0.04,0.04])
n_r, $\boldsymbol{A}$ $[-]$	3, $\boldsymbol{I}$	3, $\boldsymbol{I}$
$\boldsymbol{\phi}_b$ $[deg]$	[20, 10, 50]	[0, 0, 0]
$\boldsymbol{q}^0_m$ $[deg]$	[0,-45,0,-95,45,0]	[-6,62,0,120,4,-38,-7]
$\boldsymbol{q}^0_r$ $[deg]$	[0, 0, 0]	[0, 0, 0]
$\Delta\boldsymbol{p}^0_c$ $[m]$	[0.1, 0.3, 2.0]	[0.08, 0, 0]
r^d_{ce} $[m]$	1.5	1.5
Manipulator	CAESAR (6 DoF)	LWR (7 DOF)
$\boldsymbol{K}_c$ $[Nm]$	150 $\boldsymbol{I}$	10 $\boldsymbol{I}$
$\boldsymbol{D}_c$ $[Nms]$	1000 $\boldsymbol{I}$	40 $\boldsymbol{I}$
$\boldsymbol{K}_{ce}[Nm]$, $[Nmrad^{-1}]$	blkdiag([400 $\boldsymbol{I}$, 350 $\boldsymbol{I}$])	blkdiag([700 $\boldsymbol{I}$, 150 $\boldsymbol{I}$])
$\boldsymbol{D}_{ce}[Nms]$, $[Nmrad^{-1}s]$	blkdiag([1200 $\boldsymbol{I}$, 1100 $\boldsymbol{I}$])	blkdiag([750 $\boldsymbol{I}$, 350 $\boldsymbol{I}$])
$\boldsymbol{K}_b$ $[Nmrad^{-1}]$	500 $\boldsymbol{I}$	153 $\boldsymbol{I}$
$\boldsymbol{D}_r$ $[Nmrad^{-1}s]$	500/ $\mathbb{A}_{r\omega}$	720/ $\mathbb{A}_{r\omega}$

Alignment Phase. Given the initial CoM displacement $\Delta\boldsymbol{p}^0_c$ and the desired r^d_{ce}, the alignment is executed.

Fig. 4 illustrates how the end-effector's position and orientation evolve in order to align with and lie along $\hat{\boldsymbol{a}}^d_c$, and the convergence is also reflected in the alignment parameters evolution. The manipulator's motion induces a reaction on the satellite base (Fig. 6-left), which is compensated by the internal actuators.

Approach Phase. The approach phase is validated using the same trajectory. Since the alignment phase achieved good convergence ($r_{ce} \to r^d_{ce}$, and both $\alpha_{E\|} \to 0$ and $d_{E\perp} \to 0$) by t=100s, we initialize the CoM motion at that time. The controller generated the force required to achieve the desired system motion, depicted in Fig. 5 (left), which is shown in Fig. 5 (right). The actuation on the system leads to oscillation of the base of $< 10^{-3}$ deg (see Fig. 6), which is compensated by the reaction wheels control.

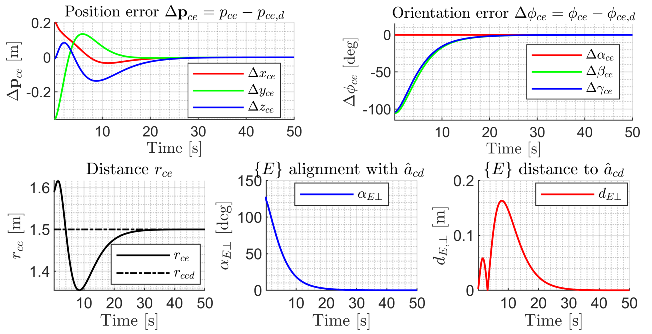

Fig. 4: *Alignment Phase*. Top: convergence of the end-effector's position $\Delta\boldsymbol{p}_{ce}$ and orientation $\Delta\boldsymbol{\phi}_{ce}$. Bottom: convergence to the parameters for the alignment performance: r_{ce}, $\alpha_{E\perp}$ and $d_{E\perp}$.

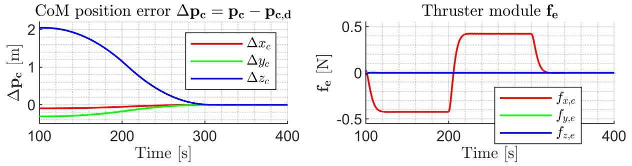

Fig. 5: *Approach Phase*. The CoM motion $\boldsymbol{p}_c$ (left) is solely relying on the control of the $\boldsymbol{f}_e$ thruster module (right).

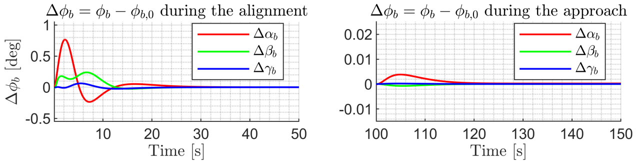

Fig. 6: Change of satellite base orientation $\boldsymbol{\phi}_b \leftarrow \boldsymbol{R}_b$ from its initial state. Left plot: alignment maneuver; right: approach.

A robustness analysis has been performed considering a number of 50 simulations with variation of 20% on the mass, 20% on the inertia and variation of the base center of mass of 5 cm. In addition, the end-effector thruster position have been altered with an uniform distribution noise of 1 cm. These results are shown in Fig. 7.

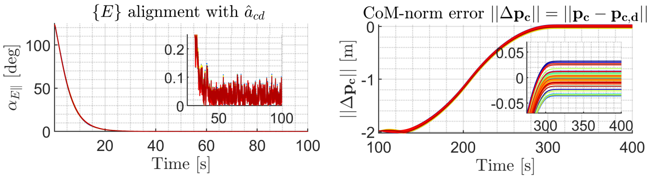

Fig. 7: Robustness analysis: Convergence error for the alignment ($\alpha_{E\perp}$, left) and CoM error norm $\Delta\boldsymbol{p}_c$ for the approach phase (right).

TABLE II: Robustness analysis: results over 50 simulations.

Parameter	Mean error	Std. dev.	Max. dev.
$\Delta\boldsymbol{p}_c$ $[m]$	0.0120	0.0101	0.0360
$\alpha_{E\|}$ $[deg]$	0.0462	0.0181	0.1174
r_{ce} $[m]$	0.0169	0.0122	0.0353
$d_{E\perp}$ $[m]$	0.52e-03	0.29e-03	1.76e-03

The maximum misalignment error is below 0.12 deg (left plot) and the maximum CoM error norm is below 0.04 m (right plot). Mean, standard deviation of the errors and maximum absolute deviation of the alignment and approach phase is summarized in Table II, as measurement of performances of the proposed control.

V. HARDWARE EXPERIMENTS

The approach has been validated through Hardware-in-the-Loop (HIL) tests in an experimental facility (OOS-Sim). The facility employs industrial robots to reproduce the 0-g dynamics. A manipulator is connected upon the chaser industrial robot and represents the arm of the scenario. The thruster module is modeled using a discrete 1 kHz signal and a time delay of 4 ms. Experiments have been performed for multiple scenarios, for both the *alignment* and the *approaching* phase sequentially. Grey boxes delimits different experiments. The supplementary video in the attachments complements the experimental results. Fig. 8 presents snapshots of the initial configuration, after alignment, and after the approach is completed.

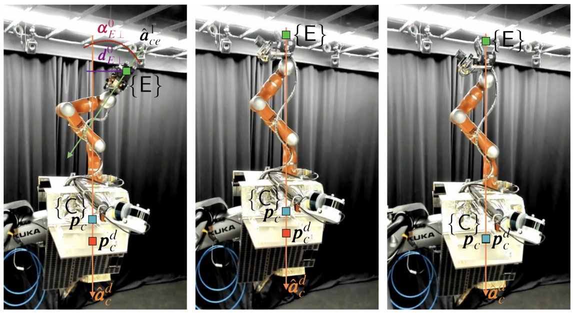

Fig. 8: Experiment in OOS-Sim. Left: start of the *alignment*, center: start of the *approach*, right: final convergence.

Alignment Phase. Once Δp^0_c and r^d_{ce} are specified, the alignment maneuver performance can be evaluated through the convergence to $\alpha_{E\perp}$, $d_{E\perp}$ and r_{ce}. To demonstrate the convergence under different conditions, we vary only the Δx_c component of $\Delta \boldsymbol{p}_c = [\Delta x_c,\, \Delta y_c,\, \Delta z_c]$ as specified in Table III, assuming $\Delta y_c = \Delta z_c = 0$ and fixing $r^d_{ce} = 1.5$ m. The initial configuration and the control parameters are in Table I.

TABLE III: Initial CoM error $\Delta \boldsymbol{p}^0_c = [\Delta x^0_c,\, 0,\, 0]$ for different experiments with respect to the last condition.

TEST	I	II	III	IV	V	VI	VII
$\Delta x^0_c\ [m]$	0.4	0.15	0.45	0.325	0.625	0.5	0.75

Fig. 9 shows the experimental results. Grey bars separate individual tests. The Δx_c distance is changed online, which is visible in the abrupt changes of the desired quantities. The results show the thruster position $\boldsymbol{p}_e$ convergence to the desired value with a maximum error of 1 cm for direction. The module alignment with $\hat{\boldsymbol{a}}^d_c$, measured by $\alpha_{E\perp}$, is reached with an accuracy of 1.8 deg, while the $d_{E\perp}$, has a maximum error of 1 cm, same accuracy as r_{ce}. These slight misalignments are due to the friction of the joints.

The manipulator motion provokes a reaction of the base attitude, visible also in Fig. 9, which maximum error is 10^{-4} deg. This is compensated by the $\boldsymbol{\tau}_r$ and $\boldsymbol{\tau}_m$, visible in Fig. 10, alongside with their alignment task control. In Fig. 10, the torque $\boldsymbol{\tau}_m$ residual is due to the friction of the manipulator.

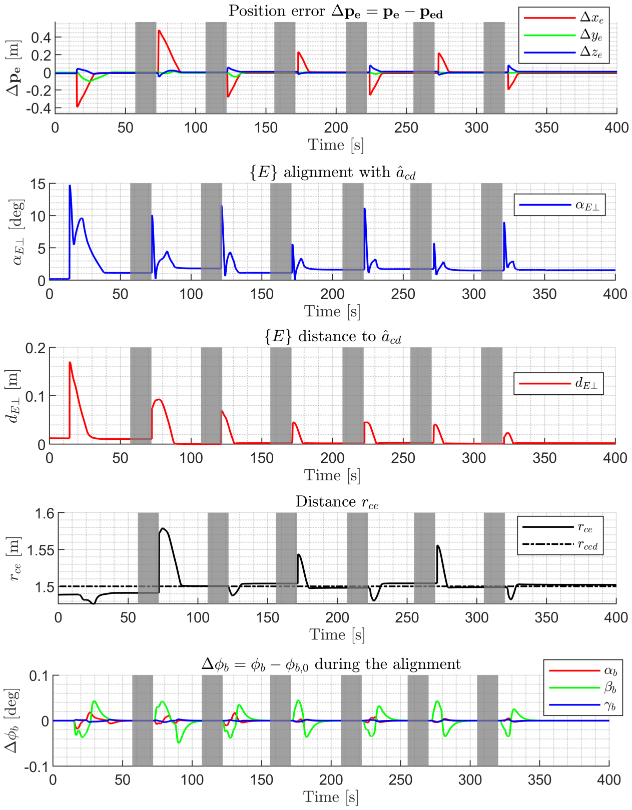

Fig. 9: *Alignment Phase*. Results of 7 different tests divided by grey boxes. Plot I: end-effector position and orientation. Plots II-III: parameters $\alpha_{E\perp}$ and $d_{E\perp}$ converges to desired null values. Plot IV: r_{ce} behaviour. Plot V: base orientation.

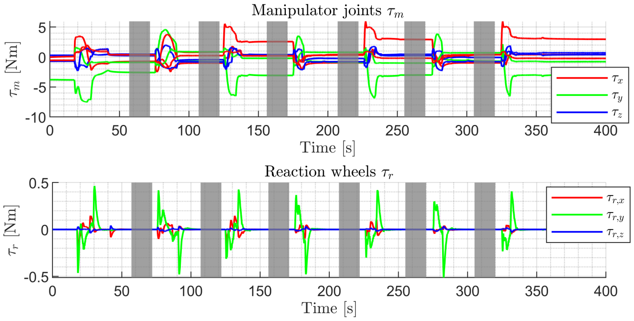

Fig. 10: *Alignment Phase*. Top: torque generated by the manipulator. Bottom: wheels torques contribution.

Approach Phase. Here, the thruster module relocates the system CoM to the desired $\boldsymbol{p}^d_c$. As in Sec. IV, the base attitude remains controlled by the actuators while a damping on the manipulator joints is active while the system moves. The CoM error $\Delta \boldsymbol{p}_c$ varies across the experiments along the z-component as shown in Table IV and visible in Fig. 8. The displacement $\Delta \boldsymbol{p}_c$ is visible in Fig. 11.

No physical thruster is present at the {E} but the same effect is provoked acting the system actuators through

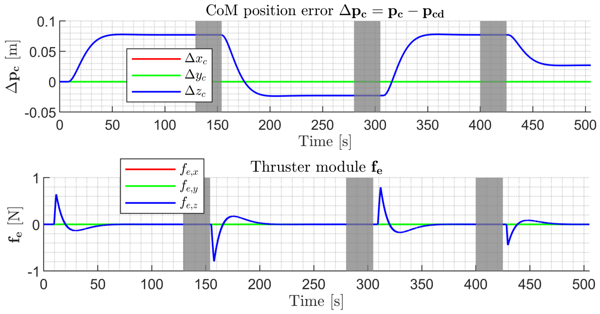

Fig. 11: *Approach Phase*. The plots show the CoM displacement (A) given the $\boldsymbol{f}_e$ actuation (B) in case of different $\boldsymbol{p}_c^d$.

TABLE IV: The initial error position $\Delta \boldsymbol{p}_c^0 = [0,\, 0,\, \Delta z_c^0]$ across the different experiments.

TEST	I	II	III	IV
$\Delta z_c^0\ [m]$	+0.08	-0.10	+0.10	-0.05

$(\boldsymbol{Ad}_{em}^T, \boldsymbol{J}_{em}^T)^T \boldsymbol{F}_e$ to produce the equivalent outcome. When a different $\boldsymbol{p}_c^d$ is selected online, the $\boldsymbol{f}_e$ present an impulsive force to accelerate the system in the opposite direction. While it approaches the target, an opposite but smaller force is continuously applied until convergence (Fig. 11).

The effect of the external actuation deals also with a non perfect convergence in the previous alignment phase. This results in a moment around the base compensated by the wheels to keep its attitude stable. The controller keeps the attitude error under 0.1 deg. The $\Delta \boldsymbol{\phi}_b$ error and the $\boldsymbol{\tau}_m$ torques are shown in Fig. 12.

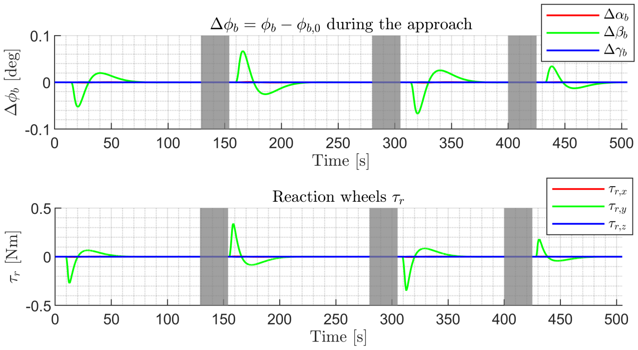

Fig. 12: Top: base-attitude error in the different tests. Bottom: reaction wheels torque needed for regulation.

VI. CONCLUSION AND FUTURE WORKS

This work proposed a control strategy for an orbital manipulator equipped with an end-effector thruster, enabling CoM maneuvers without base-mounted thrusters. The approach combines manipulator motion and end-effector actuation while maintaining base-attitude stability via reaction wheels.

Numerical experiments showed the CoM displacement and alignment to be robust to 20% variation in dynamic parameters and 1 cm variance in end-effector measurement noise. Further validation using the OOS-Sim facility demonstrated the applicability of the method with an Hardware-in-the-Loop platform.

Considering thruster limits and augmenting the controller with state observers may be scope for future work.

REFERENCES

[1] K. Yoshida, “Engineering test satellite VII flight experiments for space robot dynamics and control: theories on laboratory test beds ten years ago, now in orbit,” *The International Journal of Robotics Research*, vol. 22, no. 5, pp. 321–335, 2003.

[2] D. A. Whelan *et al.*, “DARPA Orbital Express program: effecting a revolution in space-based systems,” in *Small Payloads in Space*, vol. 4136. SPIE, 2000, pp. 48–56.

[3] T. Uhlig, F. Sellmaier, and M. Schmidhuber, *Spacecraft Operations*. Springer, 2015.

[4] X. T. Yan and G. Visentin, Eds., *Space Robotics: The State of the Art and Future Trends*. Springer Cham, 2024.

[5] H. Mishra, T. Vicariotto, and M. De Stefano, “Dynamics, simulation control of orbital modules for on-orbit assembly,” *IEEE Robotics and Automation Letters*, vol. 10, no. 1, pp. 200–207, 2025.

[6] M. Wang and Y. Xie, “Control capability analysis for complex spacecraft thruster configurations,” *Science China Technological Sciences*, vol. 53, pp. 2089–2096, 2010.

[7] A. M. Giordano, A. Dietrich, C. Ott, and A. Albu-Schäffer, “Coordination of thrusters, reaction wheels, and arm in orbital robots,” *Robotics and Autonomous Systems*, vol. 131, p. 103564, 2020.

[8] P. A. Servidia and R. S. Pena, “Spacecraft thruster control allocation problems,” *IEEE Transactions on Automatic Control*, vol. 50, no. 2, pp. 245–249, 2005.

[9] J. R. Wertz, *Spacecraft Attitude Determination and Control*. Springer Science & Business Media, 2012, vol. 73.

[10] A. Antonello *et al.*, “Dynamics and control of spacecraft manipulators with thrusters and momentum exchange devices,” *Journal of Guidance, Control, and Dynamics*, vol. 42, no. 1, pp. 15–29, 2019.

[11] A. Ruiz *et al.*, “Oru-boas: Developing reusable building blocks for satellite modularisation,” in *74th International Astronautical Congress*, 2023.

[12] M. A. Roa *et al.*, “EROSS: In-orbit demonstration of European robotic orbital support services,” in *2024 IEEE Aerospace Conference*, pp. 1–9.

[13] G. Nava *et al.*, “Position and attitude control of an underactuated flying humanoid robot,” in *2018 IEEE-RAS 18th International Conference on Humanoid Robots*, 2018, pp. 1–9.

[14] X. Sembély *et al.*, “Design and development of an electric propulsion deployable arm for Airbus Eurostar E3000 comsat platform,” in *Proc. 35th Int. Electric Propulsion Conf.*, 2017, pp. 8–12.

[15] Z. Wei *et al.*, “Electric thruster configuration design optimization for geostationary satellites with robotic manipulators,” *Advances in Space Research*, vol. 69, no. 10, pp. 3798–3813, 2022.

[16] F. Sena, H. Mishra, R. Vijayan, and M. De Stefano, “A control strategy for an orbital manipulator equipped with an external actuator at the end-effector,” in *2025 IEEE Int. Conf. on Robotics and Automation (ICRA)*, 2025, pp. 14617–14623.

[17] R. Vijayan, M. De Stefano, and C. Ott, “Control of an orbital manipulator with reaction wheels for on-orbit servicing,” *IFAC*, vol. 55, no. 38, pp. 26–32, 2022.

[18] R. M. Murray, “Proportional derivative (PD) control on the Euclidean group,” in *European Control Conference*, vol. 2, 1995, p. 1091.

[19] Y. Umetani and K. Yoshida, “Resolved motion rate control of space manipulators with generalized Jacobian matrix,” Ph.D. dissertation, Tohoku University, 1989.

[20] O. Khatib and J. Burdick, “Optimization of dynamics in manipulator design: The operational space formulation,” *Int. J. Robotics Autom.*, vol. 2, no. 2, pp. 90–98, 1987.

[21] J.-J. E. Slotine and W. Li, “On the adaptive control of robot manipulators,” *The International Journal of Robotics Research*, vol. 6, no. 3, pp. 49–59, 1987.

[22] F. Caccavale *et al.*, “Six-DOF impedance control based on angle/axis representations,” *IEEE Transactions on Robotics and Automation*, vol. 15, no. 2, pp. 289–300, 1999.

[23] A. Dietrich and C. Ott, “Hierarchical impedance-based tracking control of kinematically redundant robots,” *IEEE Transactions on Robotics*, vol. 36, no. 1, pp. 204–221, 2020.